

Research Article

Effects of Thermal Radiation and Chemical Reaction on Hydromagnetic Fluid Flow in a Cylindrical Collapsible Tube with an Obstacle

Nictor Mwamba ¹, Jeconia Okelo Abonyo,² and Kennedy Otieno Awuor ³

¹Department of Mathematics, Pan African University Institute of Basic Sciences, Technology and Innovation, Nairobi, Kenya

²Department of Pure and Applied Mathematics, Jomo Kenyatta University of Agriculture and Technology, Nairobi, Kenya

³Department of Pure and Applied Mathematics, Kenyatta University, Nairobi, Kenya

Correspondence should be addressed to Nictor Mwamba; nictor.mwamba@students.jkuat.ac.ke

Received 6 December 2022; Revised 1 February 2023; Accepted 14 February 2023; Published 3 March 2023

Academic Editor: Saranya Shekar

Copyright © 2023 Nictor Mwamba et al. This is an open access article distributed under the Creative Commons Attribution License, which permits unrestricted use, distribution, and reproduction in any medium, provided the original work is properly cited.

The aim of this research is to study the effects of thermal radiation and chemical reaction on hydromagnetic fluid flow in a cylindrical collapsible tube with an obstacle. The fluid flow is governed by continuity, momentum, energy, and concentration equations. Similarity transformation has been used to convert the obtained PDEs into ODEs. The collocation method has been used to numerically solve the ODEs. The method has been implemented in MATLAB using the `bvp4c` inbuilt function. The effects of the nondimensional parameters on velocity, temperature, and concentration have been presented graphically. Additionally, the skin-friction coefficient, the Nusselt number, and the Sherwood number have been discussed and are presented in a tabular form. The findings demonstrated that increasing the Reynolds number causes a rise in the fluid temperature and velocity. The fluid velocity decreases as the Hartmann number and the weight of the obstacle increase but increases with increasing Grashof numbers. The temperature of the fluid increases as the radiation parameter, or Eckert number, increases, but decreases as the Prandtl number increases. As the Soret number rises, so do the fluid's temperature and concentration distribution. With an increase in the unsteadiness parameter, the fluid velocity and the concentration distribution decrease, whereas the opposite is seen in temperature. As the Schmidt number, the concentration Grashof number, and the chemical reaction parameter increase, the fluid's concentration decreases. There is an increase in skin-friction coefficient with increasing Prandtl number, Eckert number, Soret number, thermal Grashof number, concentration Grashof number, thermal radiation parameter, Hartmann number, and unsteadiness parameter, while a decrease is observed with increasing Reynolds number. The Nusselt number increases with an increase in the Prandtl number, Eckert number, thermal radiation parameter, Hartmann number, and unsteadiness parameter. A slight decrease in the Nusselt number has been observed with increasing thermal Grashof number. The Sherwood number decreases with increasing Prandtl number, chemical reaction parameter, and thermal radiation parameter but increases with increasing Schmidt number, Eckert number, and Soret number. The research has the potential for a wide range of applications including but not limited to the medical field and other physical sciences.

1. Introduction

In recent years, numerous researchers have conducted in-depth studies on the flow of fluids through collapsible tubes. This is due to its wide range of biological applications, including the movement of food in the gastrointestinal tract, the airflow in the lungs, and the blood flow in the vessels.

Since blood vessels can constrict and dilate through processes known as vasoconstriction and vasodilation, respectively, it is possible to think of them as collapsible tubes.

Alsemiry et al. [1] investigated the numerical solution of blood flow and mass transport in an elastic tube with multiple stenoses. Kigo Mwangi et al. [2] analyzed an unsteady magnetohydrodynamic fluid flow in a collapsible

tube. Bég et al. [3] investigated heat and mass transfer in a micropolar axisymmetric stagnation enclosing flow with variable thermal conductivity on a cylinder.

Shaheen et al. [4] studied heat transmission in a Williamson fluid flow through a ciliated porous tube. Al-Kouz et al. [5] carried out the analysis of heat transfer and entropy generation of a hybrid magnetic nanofluid flow in a two-layered trapezoidal wavy enclosure with porous media. The unsteady flow of a Newtonian fluid through a cylindrical collapsible tube was studied by Phoebe et al. [6]. Fluid flow and heat transfer through a vertical cylindrical collapsible tube in the presence of a magnetic field and an obstacle were investigated by Chepkonga et al. [7]. Priyadharshini et al. [8] investigated the unsteady flow of collapsible tubes under transverse magnetohydrodynamic fluid. Ullah et al. [9] conducted a numerical study on a magnetized 2D hybrid nanofluid (GO + ZnO + blood) flow through a porous capillary.

In many industrial and technical processes, thermal energy transfer is crucial to controlling excessive heat generation and for protecting the systems from overheating. There are three processes through which thermal energy is transferred: convection, conduction, and radiation. Convection occurs as a result of the heated substance moving in an accumulative motion, as opposed to conduction, which includes the transmission of heat through direct contact. Thermal radiation is the process by which electromagnetic radiation transfers thermal energy. Radiative heat transfer is critical in the treatment of cancer-affected tissues [10]. Loganathan et al. [11] investigated the dynamics of a nanofluid subjected to thermal radiation, free convection, and bioconvection over an electromagnetic surface heated by convection.

In the flow of fluids, a temperature gradient may exist which can result in the phenomenon known as the Soret effect. This results in the movement of heated molecules from regions of higher temperature to regions of lower temperature. Heat and mass transfer flows involving chemical reactions are important in a variety of processes. A few of these processes include drying, geothermal pools, steel manufacturing system, oil recovery, and cooling mechanisms. Scholars have studied the transfer of heat and mass in various contexts for the reasons mentioned above and for many other reasons as well. Ferdows et al. [12] analyzed the thermal cooling performance of a convective nanofluid flowing across a moving extending surface. Alharbi et al. [13] investigated the effects of viscous dissipation and Coriolis on the heat and mass transfer of a 3D nonNewtonian fluid flow. Ali et al. [14] numerically simulated a bioconvective flow of a nanofluid over a stretching and heating surface. Thermal energy transfer characteristics during a hybrid nanofluid migration were studied by Rizk et al. [15]. The effects of mass transfer, thermal radiation, and Hall current on the Carreau fluid flow through a porous and stretching (shrinking) sheet was examined by Khan et al. [16]. Ali et al. [17] addressed the influence of a mixed convection flow and thermal radiation flow past a stretchable vertical surface on a hybrid nanofluid. Ali et al. [18] looked at the physical effects of a stretched sheet with convective heating and a Cross fluid containing

carboxymethyl cellulose. Similar research studies have been performed by several authors [19–23].

Hydromagnetics, also known as magnetohydrodynamics (MHD), is the study of the dynamics of electrically conducting fluids in magnetic fields. Examples of such fluids include electrolytes, plasmas, and liquid metals. MHD is used in a wide range of technical applications, including plasma physics, magnetic drug aiming, astronomy and astrophysics, and in electric power generation systems with high efficiency and low emissions. Ullah et al. [24] studied a magnetite-water-based nanofluid on an inclined rotating surface. The effects of thermal radiations and couple stress on the flow was considered. An analysis of the magnetized nanofluid flow in a permeable 3D tank was carried out by Shah et al. [25]. Reddy et al. [26] studied the chemical reaction impact on MHD natural convection flow through a porous medium past an exponentially stretching sheet in the presence of a heat source/sink and viscous dissipation. Prabhakar Reddy and Makinde [27] examined the unsteady hydromagnetic boundary layer flow of a reacting and radiating electrically conducting fluid past a slippery permeable vertical plate embedded in a porous medium. Elalamy et al. [28] analyzed the blood flow of MHD nonNewtonian nanofluid with heat transfer and slip effects. Ahmed et al. [29] conducted a numerical investigation of unsteady magnetohydrodynamics Eyring–Powell fluid in which thermal radiation and bioconvection were put into consideration. Salawu et al. [30] studied the flow of a magnetized hybrid Prandtl–Eyring nanofluid along the interior parabolic solar trough collector of an aircraft wing. Their focus was on thermal energy distribution, entropy generation, and fluid flow rate.

Although numerous investigations have been conducted on various areas of fluid flow through collapsible tubes and heat and mass transfer, not much attention has been given to the study of the effects of thermal radiation and chemical reactions on hydromagnetic fluid flow in a collapsible tube with an obstacle. In the present study, the work of Chepkonga et al. [7] has been extended by incorporating the effects of thermal radiation and chemical reaction on a hydromagnetic fluid flow with an obstacle. Therefore, the objective of this research is to study the effects of thermal radiation and chemical reaction on hydromagnetic fluid flow through a cylindrical collapsible tube with an obstacle. The Lorentz force, weight of the obstacle, Joule heating, Soret, and the dissipation effects have been taken into account.

2. Mathematical Formulation

Figure 1 shows a cylindrical geometric configuration with a coordinate system (r, θ, z) , where r is the radial distance, θ is the azimuthal angle, and z is the axial coordinate. The velocity components are u_z , u_θ , and u_r in the z , angular, and r direction, respectively. B_0 is a constant magnetic field. The tube's wall is $r = a_0 \sqrt{1 - \alpha_1 t}$, where α_1 is a constant of dimension $[T^{-1}]$ which characterizes the unsteadiness in the flow field and a_0 is the characteristic radius of the tube [31].

The fluid is assumed to be Newtonian, incompressible, and electrically conductive. There is no flow separation in the

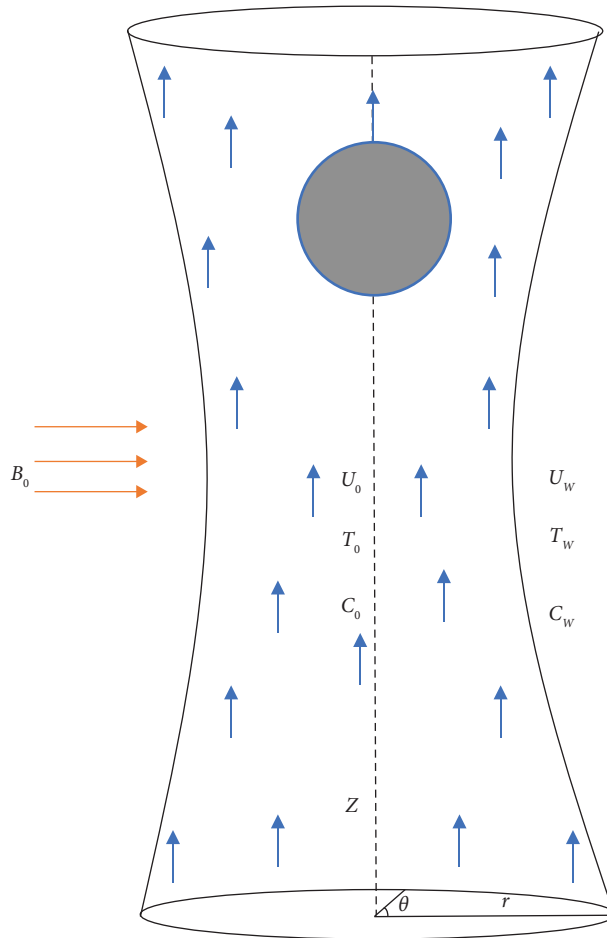


FIGURE 1: Geometry of the collapsible tube.

collapsible section of the tube and on the obstacle. The flow is laminar and unsteady. The tangential and radial directions of the flow are negligible, and no magnetic field is induced

within the fluid. The governing equations are continuity, momentum, energy, and concentration equations, which are denoted as follows [7, 32, 33]:

$$\frac{\partial u_z}{\partial z} = 0, \tag{1}$$

$$\frac{\partial u_z}{\partial t} = \beta g(T - T_w) + \beta_c g(C - C_w) + \frac{\mu}{\rho} \left[\frac{1}{r} \frac{\partial}{\partial r} \left(r \frac{\partial u_z}{\partial r} \right) \right] - \frac{\sigma B_0^2 u_z}{\rho} + \frac{4\pi r_1^3 \rho_1 g}{3\rho}, \tag{2}$$

$$\left(\frac{\partial T}{\partial t} + u_z \frac{\partial T}{\partial z} \right) = \frac{\kappa}{\rho C_p} \left(\frac{\partial^2 T}{\partial r^2} + \frac{1}{r} \frac{\partial T}{\partial r} + \frac{\partial^2 T}{\partial z^2} \right) + \frac{\mu}{\rho C_p} \left(\frac{\partial u_z}{\partial r} \right)^2 + \frac{\sigma u_z^2 B_0^2}{\rho C_p} - \frac{1}{C_p} \frac{\partial q_r}{\partial r}, \tag{3}$$

$$\frac{\partial C}{\partial t} + u_z \frac{\partial C}{\partial z} = D \left(\frac{\partial^2 C}{\partial r^2} + \frac{1}{r} \frac{\partial C}{\partial r} + \frac{\partial^2 C}{\partial z^2} \right) + \frac{D\alpha}{T_m} \left(\frac{\partial^2 T}{\partial r^2} + \frac{\partial^2 T}{\partial z^2} \right) - k_r (C - C_w), \tag{4}$$

where β , β_c , T , T_w , C , and C_w are the volumetric thermal expansion, volumetric concentration expansion, temperature, temperature at the wall, concentration, and concentration at the wall, respectively. And σ is the electrical conductivity, B_0 is the magnetic field, ρ is the fluid density, ρ_1

is the density of the obstacle, C_p is the specific heat capacity, D is the concentration of diffusion parameter, T_m is the mean temperature, α is the thermal diffusion ratio, k_r is the chemical reaction parameter, r_1 is the obstacle's radius, and κ is the thermal conductivity.

The following are the boundary conditions that have been considered:

At the center line,

$$u_z = U_0, T = T_0, C = C_0, r = 0. \quad (5)$$

At the wall,

$$u_z = 0, T = T_W, C = C_W, r = a(t). \quad (6)$$

The following similarity transformations obtained from other researchers [34–37] are used to convert the system of partial differential equations into nondimensional ordinary differential equations (ODEs):

$$u_z = -\frac{Q}{z} \frac{1}{\delta^{m+1}} f(\eta), \frac{\omega(\eta)}{\delta^{m+1}} = \frac{T - T_W}{T_0 - T_W}, \frac{\omega(\eta)_c}{\delta^{m+1}} = \frac{C - C_W}{C_0 - C_W}, \quad (7)$$

where Q is the discharge, $f(\eta)$ is the dimensionless velocity, $\omega(\eta)$ is the dimensionless temperature, and $\omega(\eta)_c$ is the dimensionless concentration. δ is a time-dependent length scale, $\eta = r/a_0$, and m is an arbitrary constant.

By the Rosseland approximation, the radiative heat flux for the thermal radiation q_r is given by [38]

$$q_r = -\frac{4\sigma_1}{3\kappa_1} \frac{\partial T^4}{\partial r}, \quad (8)$$

where σ_1 is the Stefan–Boltzmann constant and κ_1 is the mean absorption coefficient. Let the temperature variations within the flow be used to express the term T^4 as a function of the temperature [39]. This is achieved by disregarding higher-order terms and after expanding T^4 in a Taylor series of T_0 .

$$T^4 = T_0^4 + (T - T_0)4T_0^3 + \frac{(T - T_0)^2}{2!} 12T_0^2 + \dots \cong 4TT_0^3 - 3T_0^4. \quad (9)$$

Substituting the abovementioned transformations in equations (2)–(4) gives the following equations:

$$\begin{aligned} & \frac{\mu}{\rho} \frac{Q}{a_0^2 z} \frac{1}{\delta^{m+1}} f''(\eta) + \frac{\mu}{\rho} \frac{Q}{a_0^2 \eta z} \frac{1}{\delta^{m+1}} f'(\eta) + \frac{Q}{z} \frac{(m+1)}{\delta^{m+2}} \frac{d\delta}{dt} f(\eta) \\ & + \frac{\sigma B_0^2}{\rho} \left[\frac{Q}{z} \frac{1}{\delta^{m+1}} \right] f(\eta) - \beta g (T - T_W) - \beta_c g (C - C_W) - \frac{4\pi r^3 \rho_1 g}{3\rho} = 0, \end{aligned} \quad (10)$$

$$\begin{aligned} & -(T_0 - T_W) \frac{(m+1)\omega(\eta)}{\delta^{m+2}} \frac{d\delta}{dt} = \frac{\kappa}{\rho C_p} \left\{ \frac{1}{a_0^2} \left[\frac{(T_0 - T_W)\omega''(\eta)}{\delta^{m+1}} \right] + \frac{1}{a_0^2 \eta} \left[(T_0 - T_W) \frac{\omega'(\eta)}{\delta^{m+1}} \right] \right\} \\ & + \frac{\mu}{\rho C_p} \frac{Q^2}{a_0^2 z^2} \frac{1}{\delta^{2(m+1)}} (f'(\eta))^2 + \frac{\sigma B_0^2}{\rho C_p} \frac{Q^2}{z^2} \frac{1}{\delta^{2(m+1)}} f^2(\eta) + \frac{16\sigma_1 T_0^3}{3C_p \kappa_1} \frac{1}{a_0^2} \left[(T_0 - T_W) \frac{\omega''(\eta)}{\delta^{m+1}} \right], \end{aligned} \quad (11)$$

$$-\frac{(m+1)\omega(\eta)_c}{\delta^{m+2}} \frac{d\delta}{dt} = D \left[\frac{1}{a_0^2} \frac{\omega''(\eta)_c}{\delta^{m+1}} + \frac{1}{a_0^2 \eta} \frac{\omega'(\eta)_c}{\delta^{m+1}} \right] + \frac{D\alpha}{a_0^2 T_m} \frac{(T_0 - T_W)}{(C_0 - C_W)} \left[\frac{\omega''(\eta)}{\delta^{m+1}} \right] - k_r \frac{(C - C_W)}{(C_0 - C_W)}. \quad (12)$$

We introduce the dimensionless variables and quantities listed as follows [7, 32]:

$$\begin{aligned} \text{Re} &= \frac{Q\rho}{\mu} \Gamma = \frac{k_r \rho a_0^2}{\mu_0} \text{Pr} = \frac{C_p \mu}{\kappa} \text{Ec} = \frac{Q^2}{C_p \Delta T} \text{Ha} = a_0 B \sqrt{\frac{\sigma}{\mu}} \text{Gr} = \frac{g\beta(T - T_w)a_0^3}{\nu^2}, \\ \text{Sc} &= \frac{\mu}{\rho D} \text{Sr} = \frac{D\alpha(T_W - T_0)}{\nu T_m (C_W - C_0)} \lambda = \frac{\rho \delta^m}{\mu a_0^{m-1}} \frac{d\delta}{dt} \text{Rd} = \frac{16\sigma_1 T_0^3}{3\mu C_p \kappa_1} \text{Gr}_c = \frac{g\beta(C - C_w)a_0^3}{\nu^2}, \end{aligned} \quad (13)$$

where Gr is the thermal Grashof number, Pr is the Prandtl number, Rd is the thermal radiation parameter, Gr_c is the concentration Grashof number, Sr is the Soret number, and

Sc is the Schmidt number. Ha is the Hartmann number, Re is the Reynolds number, Ec is the Eckert number, Γ is the chemical reaction parameter, and λ is the unsteadiness

parameter. By substituting equation (13), in equations (10)–(12), the following set of ODEs is obtained with transformed boundary conditions:

$$f''(\eta) + \frac{1}{\eta}f'(\eta) + \frac{a_0^{m+1}(m+1)}{\delta^{m+1}}\lambda f(\eta) - \text{Ha}^2 f(\eta) - \frac{z}{\nu}[\omega(\eta)Gr + \omega(\eta)_c Gr_c] - \text{Re} \frac{a_0^2 z \delta^{m+1}}{Q^2} \frac{4\pi r_1^3 \rho_1 g}{3\rho} = 0, \quad (14)$$

$$\left(\frac{1}{\text{Pr}} + \text{Rd}\right)\omega''(\eta) + \frac{1}{\text{Pr}\eta}\omega'(\eta) + \frac{(m+1)a_0^{m+1}}{\delta^{m+1}}\lambda\omega(\eta) + \frac{\text{Ec}}{z^2\delta^{m+1}}(f'(\eta))^2 + \frac{\text{Ha}^2}{z^2}\frac{\text{Ec}}{\delta^{m+1}}f^2(\eta) = 0, \quad (15)$$

$$\frac{1}{\text{Sc}}\frac{\omega''(\eta)_c}{\delta^{m+1}} + \frac{1}{\text{Sc}}\frac{\omega'(\eta)_c}{\eta\delta^{m+1}} + \left[\frac{a_0^{m+1}(m+1)}{\delta^{2(m+1)}}\lambda - \Gamma\frac{1}{\delta^{m+1}}\right]\omega(\eta)_c + \text{Sr}\frac{\omega''(\eta)}{\delta^{m+1}} = 0. \quad (16)$$

The transformed boundary conditions are as follows. At the center line,

$$f(0) = -z\delta^{m+1}\omega(0) = \delta^{m+1} \quad \omega(0)_c = \delta^{m+1}, \text{ if } \eta = 0. \quad (17)$$

At the wall,

$$f(\eta) = 0 \quad \omega(\eta) = 0 \quad \omega(\eta)_c = 0, \text{ if } \eta = a(t), \quad (18)$$

The skin-friction coefficient, the Nusselt number, and the Sherwood number are defined by the following relations, respectively [40]:

$$C_f = \frac{\tau_w}{\rho U_0^2}, \text{Nu} = \frac{a_0 q_w}{k(T_0 - T_w)}, \text{Sh} = \frac{a_0 q_m}{D(C_0 - C_w)}, \quad (19)$$

where τ_w is the skin shear stress on the surface, q_w is the heat flux, and q_m is the mass flux which is defined by the following equation:

$$\tau_w = \mu \frac{\partial u}{\partial r}\Big|_{r=0}, q_w = -k \frac{\partial T}{\partial r}\Big|_{r=0}, q_m = -D \frac{\partial C}{\partial r}\Big|_{r=0}. \quad (20)$$

By substituting equations (7) and (20) in equation (19), the following quantities are obtained:

$$C_f = \text{Re}^{-1} f(\eta)', \text{Nu} = \frac{-\omega(\eta)'}{\delta^{m+1}}, \text{Sh} = \frac{-\omega(\eta)'_c}{\delta^{m+1}}. \quad (21)$$

3. Numerical Solution

In order to find the numerical solutions for the obtained ODEs, the MATLAB boundary value problem solver function bvp4c is used. The bvp4c function in MATLAB is based on a collocation method that involves selecting a set of discrete points, or collocation points, in the interval of interest and requiring that the solution satisfy the differential equation at those points. The equations (14)–(16) are converted into a system of first-order ODEs as required by the bvp4c MATLAB function. Figure 2 shows the flowchart for the numerical scheme for bvp4c.

The book by Shampine et al. [41] contains additional information on the bvp4c procedure. The following conventions are used to reduce the ODEs from the second-order to the first-order:

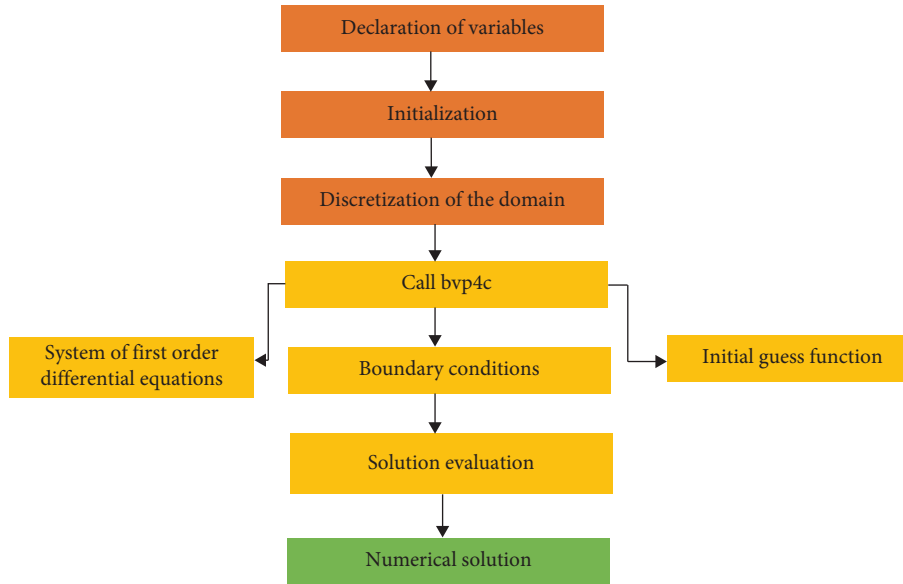


FIGURE 2: Flowchart of numerical scheme (bvp4c).

$$f(\eta) = y_1, f'(\eta) = y_2, \omega(\eta) = y_3,$$

$$\omega'(\eta) = y_4, \omega(\eta)_c = y_5, \omega'(\eta)_c = y_6,$$

$$lpc \begin{bmatrix} y_1' \\ y_2' \\ y_3' \\ y_4' \\ y_5' \\ y_6' \end{bmatrix} = \begin{bmatrix} y_2 \\ \text{Ha}^2 y_1 + \frac{z}{\nu} [y_3 Gr + y_5 Gr_c] - \frac{1}{\eta} y_2 - \frac{a_0^{m+1} (m+1)}{\delta^{m+1}} \lambda y_1 + \text{Re} \frac{a_0^2 z \delta^{m+1}}{Q^2} \frac{4\pi r_1^3 \rho_1 g}{3\rho} \\ y_4 \\ \left(\frac{1}{\eta} y_4 - \frac{\text{Pr} (m+1) a_0^{m+1}}{\delta^{m+1}} \lambda y_3 - \frac{\text{PrEc}}{z^2 \delta^{m+1}} y_2^2 - \frac{\text{PrHa}^2}{z^2} \frac{\text{Ec}}{\delta^{m+1}} y_1^2 \right) \frac{1}{1 + \rho \text{RdPr}} \\ y_6 \\ \text{Sc} \left[\Gamma - \frac{a_0^{m+1} (m+1)}{\delta^{(m+1)}} \lambda \right] y_5 - \frac{y_6}{\eta} - \text{ScSr} y_4' \end{bmatrix}. \tag{22}$$

With the following boundary conditions at the center and at the wall, respectively, we get

$$\begin{aligned} y_1 = -z\delta^{m+1}, & \quad y_3 = \delta^{m+1}, & \quad y_5 = \delta^{m+1}, \\ y_1 = 0, & \quad y_3 = 0, & \quad y_5 = 0. \end{aligned} \tag{23}$$

4. Results and Discussion

The impacts of different dynamical parameters on the quantities of interest are studied using graphical plots and tables in this section.

4.1. Velocity Profiles. Figures 3–7 are plotted to show the effects of Reynolds number Re , Grashof number Gr and Gr_c , Hartmann number Ha , chemical reaction parameter Γ , and unsteadiness parameter λ .

Figure 3 shows that an increase in the value of the Reynolds number results in an increase in the primary fluid velocity. When the Reynolds number increases, the inertial forces in the fluid become dominant over the viscous forces that oppose the fluid motion. As a result, the momentum boundary layer becomes thinner, allowing the fluid to flow more easily. From a physical point of view, the fluid velocity reduces as you move from the center of the tube to its wall. This can be attributed to the high viscous forces at the wall that resists the fluid motion.

Both Figures 4 and 5 demonstrate that an increase in the Grashof numbers leads to an increase in velocity profiles. High values of the thermal Grashof number indicate a high-temperature gradient, resulting in a greater buoyancy force that drives the fluid motion. This effect enhances the fluid velocity while simultaneously thinning the momentum boundary layer. Due to higher temperatures at the center and lower temperatures at the wall, there is a greater buoyancy force acting on the fluid at the center compared to the force at the wall. The concentration Grashof number exhibits a similar behavior, as seen in Figure 5.

From Figure 6, it has been found that increasing the Hartmann number causes a decrease in the velocity profiles, and decreasing the Hartmann number causes an increase in the velocity profiles. Increasing the Hartmann number causes an increase in the Lorentz force which causes the fluid's motion to slow down. Therefore, the Hartmann number reduces the fluid velocity while increasing the thickness of the boundary layer.

Figure 7 indicates that the velocity tends to reduce as the unsteadiness parameter increases. This is because the velocity has an inverse proportion to the time-dependent length scale, δ , which is directly proportional to the unsteadiness parameter λ . Furthermore, an increase in the unsteadiness parameter denotes that the boundary layer has pushed into the flow region, thus increasing the viscous drag forces and lowering the fluid velocity.

According to Figure 8, increasing the weight of the obstacle by increasing its density reduces fluid velocity. Increased density of the obstacle signifies an increase in the sphere's weight pushing against the direction of the flow. This retards the velocity of the fluid. Physically, the highest velocity is between the obstacle and the tube's wall.

4.2. Temperature Profiles. Increasing the Reynolds number causes an increase in the fluid temperature as shown in Figure 9. This is because increasing the Reynolds number leads to dominant inertia forces which leads to an increased fluid velocity. Apart from dissipation heating, if the magnetic field is present, increased fluid velocity results in an enhanced Joule heating that leads to temperature increase. Furthermore, the fluid temperature reduces towards the wall from the center. This is due to the difference in the fluid

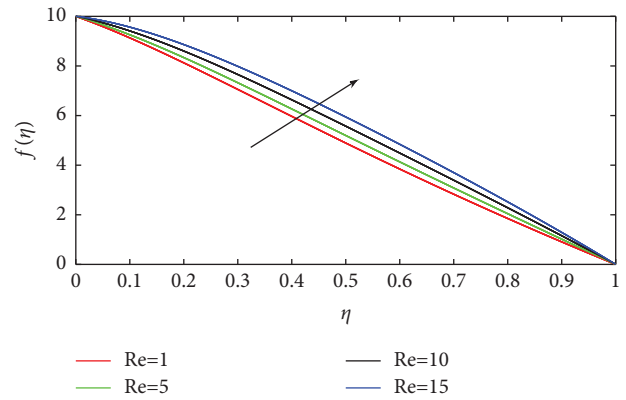


FIGURE 3: Velocity profiles for the different values of Re .

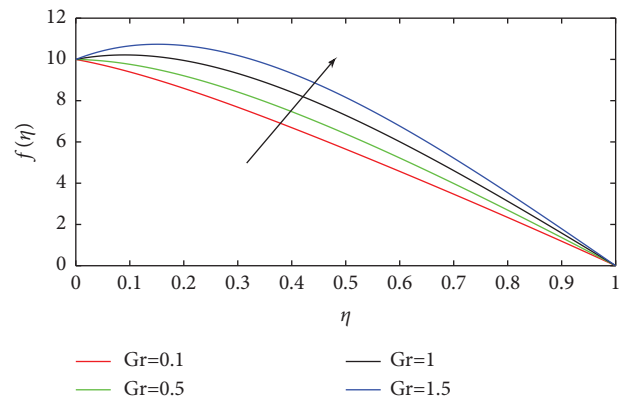


FIGURE 4: Velocity profiles for the different values of Gr .

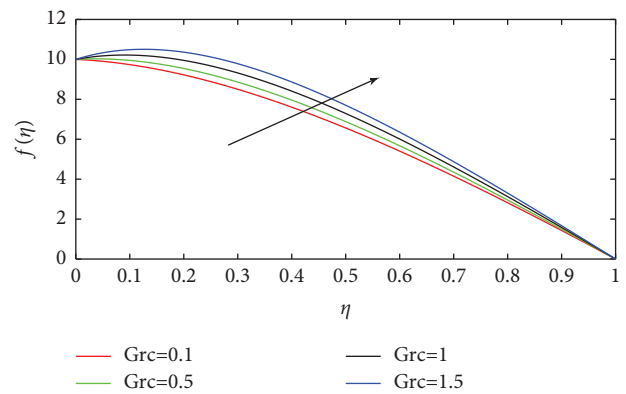


FIGURE 5: Velocity profiles for the different values of Gr_c .

velocity and viscosity which affects the fluids' internal heating abilities.

In Figure 10, the fluid temperature drops as the Prandtl number increases. This is because an increase in the Prandtl number indicates that thermal diffusivity has become less dominant. Higher values of the Prandtl number decrease the thermal boundary layer thickness. This leads to a rapid travel of heat, resulting in a fluid temperature decrease.

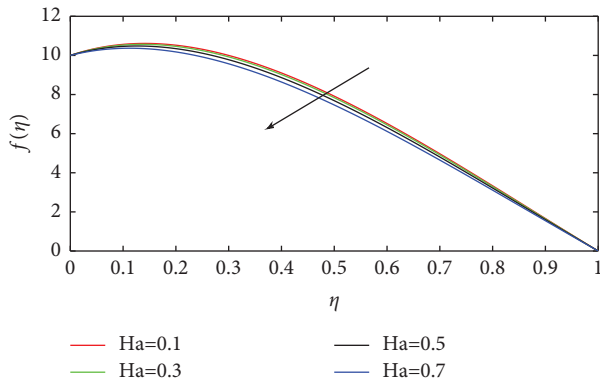


FIGURE 6: Velocity profiles for the different values of Ha.

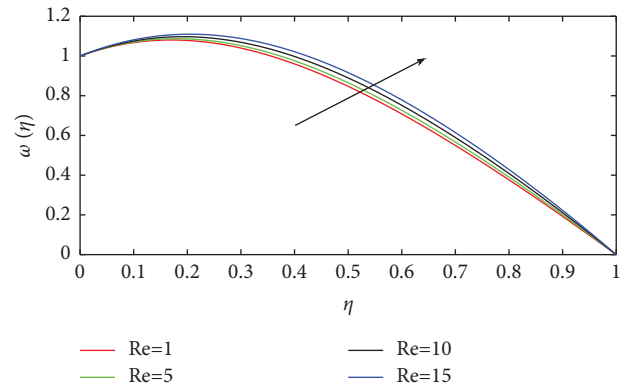


FIGURE 9: Temperature profiles for the different values of Re.

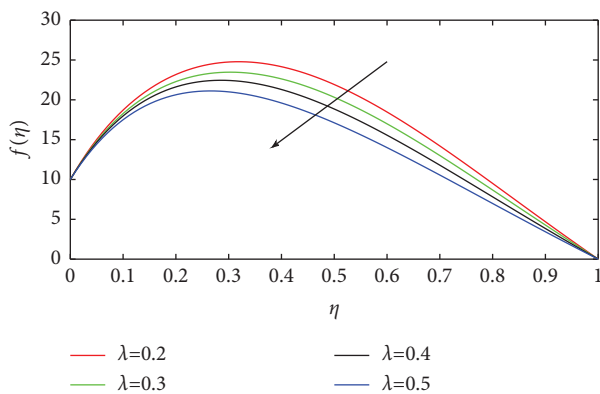


FIGURE 7: Velocity profiles for the different values of λ .

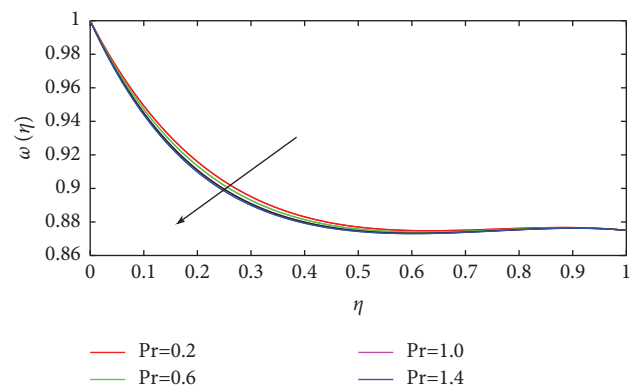


FIGURE 10: Temperature profiles for the different values of Pr.

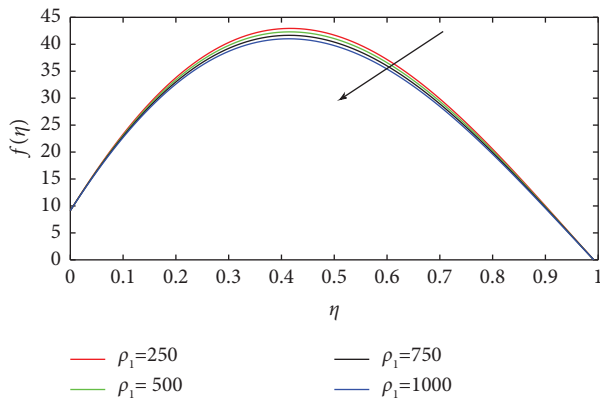


FIGURE 8: Velocity profiles for the different values of ρ_1 .

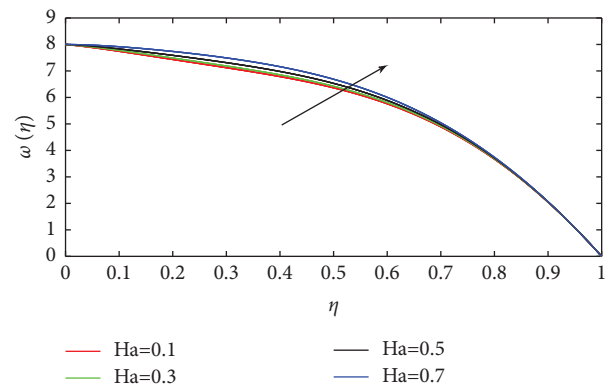


FIGURE 11: Temperature profiles for the different values of Ha.

The temperature profile shown in Figure 11 implies that increasing the Hartmann number raises the fluid temperature. This is due to the Lorentz force, which is created when a magnetic field is applied to an electrically conducting fluid flow. The Lorentz force increases as the Hartmann number increases, raising the temperature of the fluid. The temperature drops towards the wall of the tube. This is due to the low velocities near the wall which results in a low Lorentz force.

Figure 12 shows that as the Eckert number increases, the fluid temperature also increases. This is because an increase

in the Eckert number implies an increase in fluid velocity, which helps the fluid's viscous dissipation. The velocity is highest at the tube's center and so is the dissipation effect. The dissipation effect gets less noticeable at low velocity as you go closer to the wall. Also, the surface heat transfer rate is low, and the thickness of the thermal boundary layer grows.

Figure 13 shows that increasing the value of the radiation parameter causes an increase in the temperature profile of the flow. This is because increasing the radiation parameter releases heat energy into the fluid. This fits with the radiation

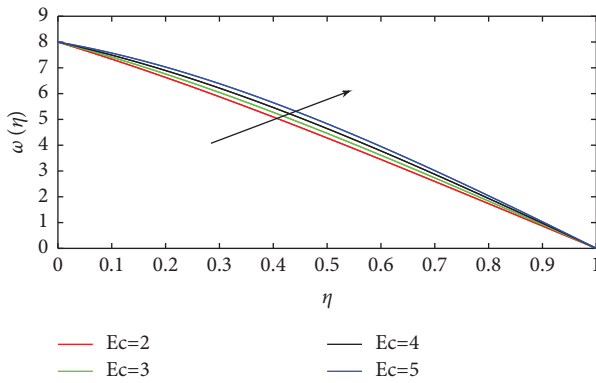


FIGURE 12: Temperature profiles for the different values of Ec.

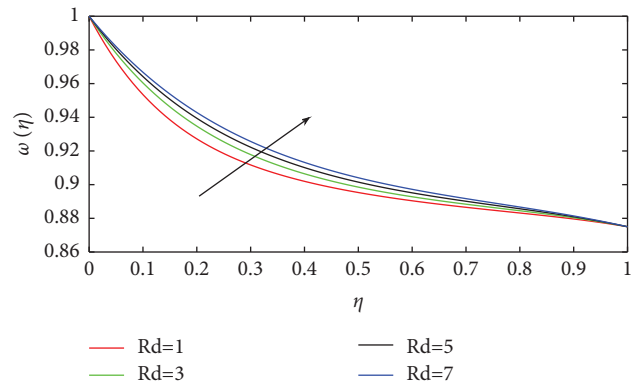


FIGURE 13: Temperature profiles for the different values of Rd.

parameter's basic physical behavior. Growing values of radiation parameter also increases the thermal boundary layer which gives an increasing effect on temperature.

Increasing the Soret number causes an increase in the fluid's temperature as shown in Figure 14. This is because increasing the Soret number implies that the temperature gradient is significant. Thus, more fluid particles will move from a region of higher temperature to regions of low temperature, thereby increasing the temperature of the fluid.

According to Figure 15, as the unsteadiness parameter increases, so does the temperature. From equations (7) and (13), it is seen that λ is directly proportional to the temperature of the fluid. As a result, increasing this parameter causes an increase in the temperature profile. Furthermore, the boundary layer tends to be at the tube's center line, which is in accordance with the increase in the unsteadiness parameter. This increases the viscous dissipation effect which in turn produces thermal energy that increases the fluid's temperature.

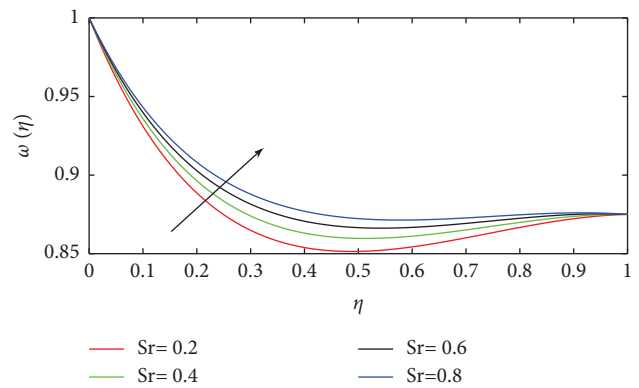


FIGURE 14: Temperature profiles for the different values of Sr.

4.3. Concentration Profiles. The concentration field decreases with increasing Schmidt number. Increasing the Schmidt number implies that mass transfer is less efficient compared to momentum transfer.

Therefore, the mass diffusion decreases and the concentration distribution decreases, so is its profile as shown in Figure 16. Physically, the momentum diffusivity at the tube's center is more than the momentum diffusivity towards the wall.

It is found from Figure 17 that the concentration of the fluid medium increases with an increase in the Soret number. Increasing the Soret numbers correspond to an increase in temperature gradients, which results in a higher convective flow. As a result, concentration distribution enhances. Since the temperature gradient is lessening as one approaches the wall, the Soret effect diminishes. Increasing the Soret number leads to a thinner concentration boundary layer.

The concentration decreases as the unsteadiness parameter increases, as shown in Figure 18. Increasing the unsteadiness parameter results in an increase in temperature which then increases the rate of a chemical reaction that leads to the reduction of concentration.

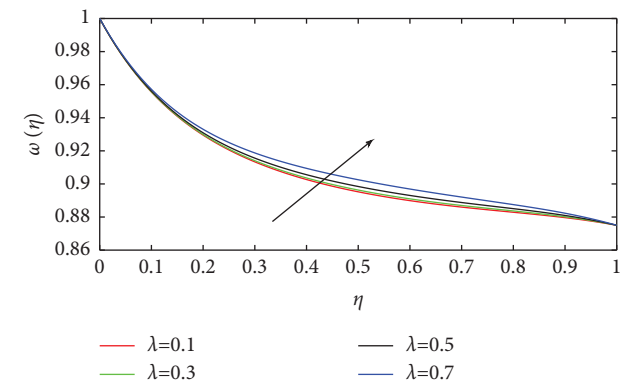


FIGURE 15: Temperature profiles for the different values of λ .

From Figure 19, it is seen that an increase in the value of the concentration Grashof number implies an increase in the concentration gradient. The Grashof number tends to boost the mass buoyancy effect. This causes an increase in the induced flow and, as a result, a decrease in concentration. Hence, the decrease in the concentration profile is shown in Figure 19. The mass buoyancy effect is strongest at the center of the tube due to the presence of a high concentration gradient. However, the mass buoyancy effect is less towards the wall.

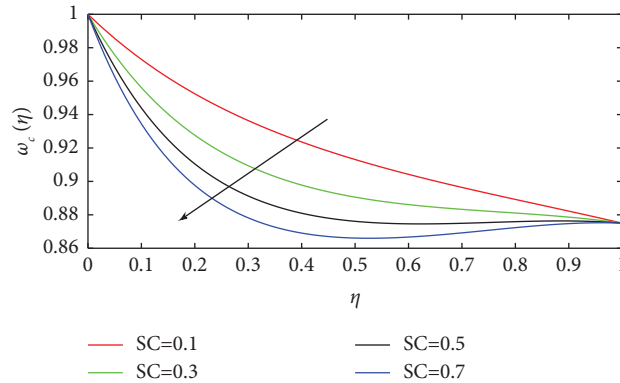


FIGURE 16: Concentration profiles for the different values of Sc.

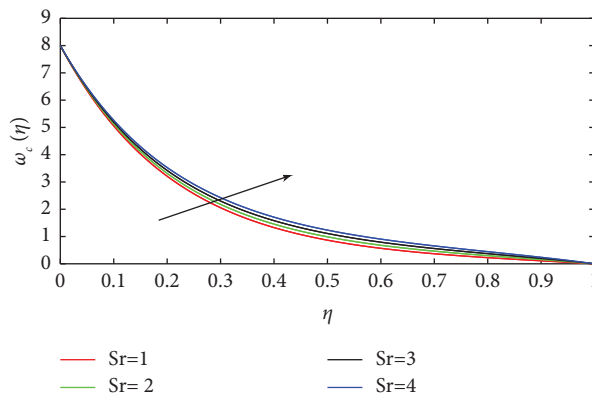


FIGURE 17: Concentration profiles for the different values of Sr.

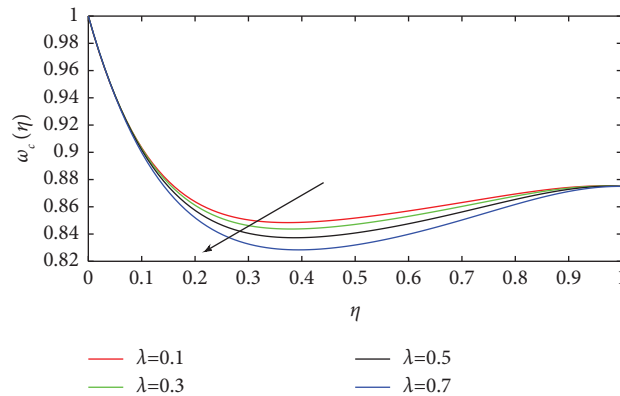


FIGURE 18: Concentration profiles for the different values of λ.

Chemical molecular diffusivity decreases with increasing chemical reaction parameters due to the consumption of the species in the reaction. Therefore, it is found from Figure 20 that the concentration field shrinks as the chemical reaction parameter increases.

4.4. *Effects of Variation of Parameters on Skin Friction.* From Table 1, it can be observed that when the Reynolds number is increased, the skin friction decreases. This is due to reduced viscous forces. There is an increase in the skin-friction coefficient with an increase in the Prandtl number

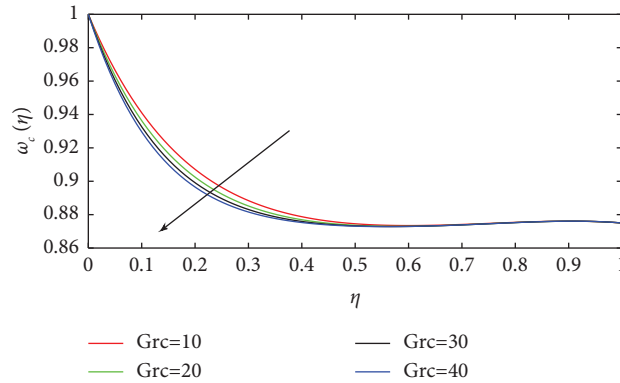


FIGURE 19: Concentration profiles for the different values of Grc.

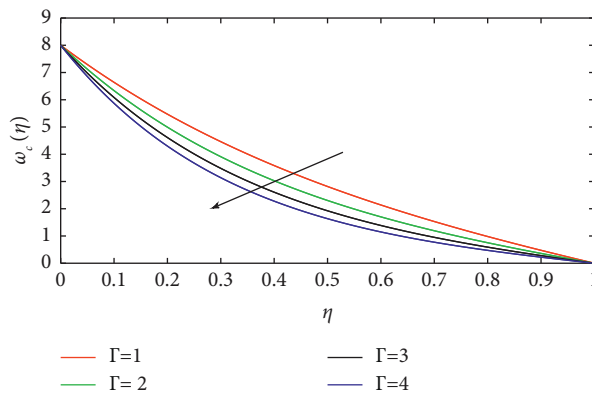


FIGURE 20: Concentration profiles for the different values of Γ .

TABLE 1: Skin-friction coefficient for various values of parameters.

Pr	Ec	Sc	Sr	Re	Γ	λ	Gr	Gc	Rd	Ha	C_f
0.71	0.01	0.02	1	1	0.1	0.2	1	1	0.1	0.01	0.045817
2	0.01	0.02	1	1	0.1	0.2	1	1	0.1	0.01	0.046146
0.71	1	0.02	1	1	0.1	0.2	1	1	0.1	0.01	0.045839
0.71	0.01	1.5	1	1	0.1	0.2	1	1	0.1	0.01	0.046001
0.71	0.01	0.02	2	1	0.1	0.2	1	1	0.1	0.01	0.04582
0.71	0.01	0.02	1	5	0.1	0.2	1	1	0.1	0.01	0.04153
0.71	0.01	0.02	1	1	1.2	0.2	1	1	0.1	0.01	0.045817
0.71	0.01	0.02	1	1	0.1	2	1	1	0.1	0.01	0.048195
0.71	0.01	0.02	1	1	0.1	0.2	10	1	0.1	0.01	0.130926
0.71	0.01	0.02	1	1	0.1	0.2	1	10	0.1	0.01	0.046167
0.71	0.01	0.02	1	1	0.1	0.2	1	1	1.5	0.01	0.046167
0.71	0.01	0.02	1	1	0.1	0.2	1	1	0.1	1.2	0.050587

and Eckert number. This can be attributed to the increased fluid momentum. An increase in the Soret number results in increased skin friction as it accelerates fluid motion. Furthermore, the thermal and concentration Grashof numbers, radiation parameters, and Hartmann numbers cause the skin friction to increase as they increase.

4.5. *Effects of Variation of Parameters on Heat Transfer Rate.* Table 2 shows the observable effects of various parameters on the Nusselt number. Increasing the Prandtl number leads to

an increase in the Nusselt number. The Nusselt number increases with an increase in the Eckert number, unsteadiness parameter, radiation parameter, and Hartmann number. These nondimension numbers increase the fluid temperature which results in enhanced heat transfer. There is little or no change in the Nusselt number when the Schmidt number, Soret number, chemical reaction parameter, Reynolds number, or concentration Grashof number is altered. However, the Nusselt number slightly decreases when the thermal Grashof number is increased.

TABLE 2: Nusselt number for various values of parameters.

Pr	Ec	Sc	Sr	Re	Γ	λ	Gr	Gc	Rd	Ha	Nu
0.71	0.01	0.02	1	1	0.1	0.2	1	1	0.1	0.01	-7.487115
2	0.01	0.02	1	1	0.1	0.2	1	1	0.1	0.01	-7.813861
0.71	1	0.02	1	1	0.1	0.2	1	1	0.1	0.01	-7.504474
0.71	0.01	1.5	1	1	0.1	0.2	1	1	0.1	0.01	-7.487115
0.71	0.01	0.02	2	1	0.1	0.2	1	1	0.1	0.01	-7.487115
0.71	0.01	0.02	1	10	0.1	0.2	1	1	0.1	0.01	-7.487114
0.71	0.01	0.02	1	1	1.2	0.2	1	1	0.1	0.01	-7.487115
0.71	0.01	0.02	1	1	0.1	2	1	1	0.1	0.01	-7.487123
0.71	0.01	0.02	1	1	0.1	0.2	10	1	0.1	0.01	-7.487114
0.71	0.01	0.02	1	1	0.1	0.2	1	10	0.1	0.01	-7.487115
0.71	0.01	0.02	1	1	0.1	0.2	1	1	1.5	0.01	-7.964663
0.71	0.01	0.02	1	1	0.1	0.2	1	1	0.1	1.2	-7.487117

TABLE 3: Sherwood number for various values of parameters.

Pr	Ec	Sc	Sr	Re	Γ	λ	Gr	Gc	Rd	Ha	Sh
0.71	0.01	0.02	1	1	0.1	0.2	1	1	0.1	0.01	-0.00562
2	0.01	0.02	1	1	0.1	0.2	1	1	0.1	0.01	-0.004368
0.71	1	0.02	1	1	0.1	0.2	1	1	0.1	0.01	-0.005652
0.71	0.01	1.5	1	1	0.1	0.2	1	1	0.1	0.01	-0.152517
0.71	0.01	0.02	2	1	0.1	0.2	1	1	0.1	0.01	-0.007609
0.71	0.01	0.02	1	5	0.1	0.2	1	1	0.1	0.01	-0.00562
0.71	0.01	0.02	1	1	1.2	0.2	1	1	0.1	0.01	-0.005613
0.71	0.01	0.02	1	1	0.1	2	1	1	0.1	0.01	-0.00562
0.71	0.01	0.02	1	1	0.1	0.2	10	1	0.1	0.01	-0.00562
0.71	0.01	0.02	1	1	0.1	0.2	1	10	0.1	0.01	-0.00562
0.71	0.01	0.02	1	1	0.1	0.2	1	1	1.5	0.01	-0.003773
0.71	0.01	0.02	1	1	0.1	0.2	1	1	0.1	1.2	-0.00562

TABLE 4: Nusselt number for various values of Re and Pr.

Re	Pr	Odejide et al. [31]	Present
1	0.71	-1.5148	-1.5195
1.5	0.71	-0.98969	-1.0057
2	0.71	-0.1096	-0.1095
1	1	-1.5208	-1.5218
1	1.5	-1.5312	-1.5361

4.6. Effects of Variation of Parameters on Mass Transfer Rate.

It has been shown in Table 3 that when the Prandtl number, chemical reaction parameter, or the radiation parameter is raised, the Sherwood number is reduced. On the other hand, the Sherwood number is enhanced when the Eckert, Schmit, or Soret number is raised. However, there is little or no effect of the Reynolds number, unsteadiness parameter, Grashof number, or Hartmann number on the Sherwood number.

4.7. *Validation.* Comparing the results obtained from the present study and that of the Odejide et al.'s [31], on the effects of the Reynolds number and the Prandtl number on the Nusselt number. It is clear from Table 4 that the two results are in close agreement.

5. Conclusion

This study has investigated the effects of thermal radiation and chemical reaction on hydromagnetic fluid flow through a cylindrical collapsible tube with an obstacle.

The research study has developed a set of mathematical equations to model hydromagnetic fluid flow in a cylindrical collapsible tube with an obstacle. The developed equations were nonlinear partial differential equations which were later converted to nonlinear ordinary differential equations and solved by using the `bvp4c` in MATLAB. The results have shown that the equations can be used to predict fluid flow behavior under various conditions. The obtained model has significant implications for the field as it provides a framework for understanding and predicting hydromagnetic fluid

flow in similar systems. However, it is important to note that the equations are based on certain assumptions and limitations.

Furthermore, this study has determined the velocity, temperature, and concentration profiles of the flow for a conductive fluid in a cylindrical collapsible tube with an obstacle, in the presence of a magnetic field. The effects of various nondimensional parameters on velocity, temperature, and concentration have been determined and the results are presented graphically. Additionally, the skin-friction coefficient, the Nusselt number, and the Sherwood number have been obtained using Maple, and are presented in tabular form.

The results showed that increasing the Reynolds number leads to an increased fluid velocity and temperature. While the fluid velocity decreases with increasing Hartmann and obstacle's weight, it increases with rising Grashof numbers. The fluid temperature rises with an increase in the radiation parameter or Eckert number but drops with an increase in the Prandtl number. The temperature and concentration distribution of the fluid increases with increased Soret number. The fluid velocity and concentration distribution decreases with increasing unsteadiness parameter, while the opposite is observed with temperature. The concentration of the fluid decreases with increasing Schmidt number, concentration Grashof number, and chemical reaction parameter.

The skin-friction coefficient increases when the Prandtl number, Eckert number, Soret number, thermal Grashof number, concentration Grashof number, thermal radiation parameter, Hartmann number, and unsteadiness parameter rise, whereas it decreases as the Reynolds number rises. Increases in the Prandtl number, Eckert number, thermal radiation parameter, Hartmann number, and unsteadiness parameter raise the Nusselt number. With the rising thermal Grashof number, the Nusselt number decreases slightly. The Sherwood number drops when the Prandtl number, chemical reaction parameter, and thermal radiation parameter rise, whereas it increases as the Schmidt number, Eckert number, and Soret number decrease.

The results obtained in this research study have the potential to be applied in the medical field, i.e., understanding blood flow in blood vessels in the presence of fat deposits and also in the treatment of thrombosis. It can also be applied in targeted drug-aiming procedures. Additionally, the blood flow can be temporarily lowered by applying a magnetic field in order to minimize the excessive blood loss.

Further work can be performed on a three-dimensional MHD fluid flow by considering a nonNewtonian turbulent flow with a varying magnetic field, incorporating both Soret and Dufour effects.

Abbreviations

MHD: Magnetohydrodynamics
ODE: Ordinary differential equation
PDE: Partial differential equation.

List of Symbols

$f(\eta)$: Dimensionless velocity
 α : Thermal diffusion ratio, (m^2s^{-1})
 α_1 : Constant of dimension T^{-1} , seconds (s)
 β : Volumetric thermal expansion, kelvin (K^{-1})
 β_c : Volumetric concentration expansion, (kgm^{-3})
 δ : Time-dependent length scale, (M)
 η : Dimensionless radius
 Γ : Chemical reaction parameter
 κ : Thermal conductivity, ($W m^{-1}K^{-1}$)
 κ_1 : Mean absorption coefficient, (m^2/mol)
 λ : Unsteadiness parameter
 μ : Fluid viscosity, ($kgm^{-1}s^{-1}$)
 ν : Kinematic viscosity, (m^2s^{-1})
 $\omega(\eta)$: Dimensionless temperature
 $\omega(\eta)_c$: Dimensionless concentration
 ρ : Density, (kgm^{-3})
 ρ_1 : Density of the obstacle, (kgm^{-3})
 σ : Electric conductivity, siemens per meter ($S \cdot m^{-1}$)
 τ_w : Skin shear stress, ($N \cdot m^2$)
 θ : Azimuthal angle, degrees
 a_0 : Characteristic radius, meters (m)
 B_0 : Constant magnetic field, Tesla (T)
 C : Concentration, mole per cubic meter mol/m^3
 C_0 : Concentration at the center, mole per cubic meter mol/m^3
 C_f : Skin-friction coefficient
 C_p : Specific heat capacity, ($Jkg^{-1}K^{-1}$)
 C_w : Concentration at the wall, mole per cubic meter mol/m^3
 D : Concentration diffusion parameter, (m^2s^{-1})
 Ec : Eckert number
 g : Gravitational constant, (Nm^2kg^{-2})
 Gr : Thermal Grashof number
 Gr_c : Concentration Grashof number
 Ha : Hartmann number
 k_r : Chemical reaction parameter, ($M \cdot s^{-1}$)
 m : Arbitrary constant
 Nu : Nusselt number
 Pr : Prandtl number
 Q : Discharge, (m^3s^{-1})
 q_m : Mass flux, ($kgm^{-2}s^{-1}$)
 q_r : Radiative heat flux, joules (J)
 q_w : Heat flux, ($W \cdot m^{-2}$)
 r : Radius of the tube, meters (m)

r_1 :	Radius of the obstacle, (m)
Rd:	Radiative parameter
Re:	Reynolds number
Sc:	Schmidt number
Sh:	Sherwood number
Sr:	Soret number
T :	Temperature, kelvin (K)
t :	Time, seconds (s)
T_0 :	Temperature at the center, kelvin (K)
T_m :	Mean temperature, kelvin (K)
T_w :	Temperature at the wall, kelvin (K)
u_z, u_θ, u_r :	Velocity components, (ms^{-1})
z :	Axial coordinate, meters (m).

Data Availability

The data used to support the findings of this study are available within the article and are also available from the corresponding author upon request.

Conflicts of Interest

The authors declare that they have no conflicts of interest.

Acknowledgments

The authors are grateful to the Pan African University Institute of Basic Science, Technology and Innovation (PAUSTI) for their support throughout the conduct of the study. The authors also appreciate the Jomo Kenyatta University of Agriculture Science and Technology for hosting PAUSTI. This research was funded by the African Union through The Pan African University, Institute for Basic Science, Technology and Innovation.

References

- [1] R. D. Alsemiry, P. K. Mandal, P. K. Mandal, H. M. Sayed, and N. Amin, "Numerical solution of blood flow and mass transport in an elastic tube with multiple stenoses," *BioMed Research International*, vol. 2020, Article ID 7609562, 14 pages, 2020.
- [2] J. Kigo Mwangi, M. N. Kinyanjui, K. Giterere, and P. Kiogora, "Unsteady magnetohydrodynamic fluid flow in a collapsible tube," *International Journal of Engineering Science and Innovative Technology*, vol. 4, no. 5, pp. 111–118, 2015.
- [3] O. A. Bég, R. Bhargava, S. Sharma, T. A. Bég, M. Shamshuddin, and A. Kadir, "Numerical solutions for axisymmetric non-Newtonian stagnation flow, heat, and mass transfer with application to cylindrical pipe coating dynamics," *Computational Thermal Sciences: International Journal*, vol. 12, no. 1, pp. 79–97, 2020.
- [4] S. Shaheen, S. Shaheen, M. Arain et al., "A case study of heat transmission in a Williamson fluid flow through a ciliated porous channel: a semi-numerical approach," *Case Studies in Thermal Engineering*, vol. 41, no. 523, Article ID 102523, 2023.
- [5] W. Al-Kouz, A. Abderrahmane, M. Shamshuddin et al., "Heat transfer and entropy generation analysis of water- fe_3o_4/cnt hybrid magnetic nanofluid flow in a trapezoidal wavy enclosure containing porous media with the galerkin finite element method," *The European Physical Journal Plus*, vol. 136, no. 11, p. 1184, 2021.
- [6] M. Phoebe, G. Kangethe, and K. Roy, "Unsteady flow of a Newtonian fluid through a cylindrical collapsible tube," *International Journal of Advances in Applied Mathematics and Mechanics*, vol. 1, 2019.
- [7] D. Chepkonga, K. Roy, and G. Kangethe, "Fluid flow and heat transfer through a vertical cylindrical collapsible tube in the presence of magnetic field and an obstacle," *International Journal of Advances in Applied Mathematics and Mechanics*, 2019.
- [8] S. Priyadharsinia, M. Suvitha, T. Priya, K. Preethi, and R. Nivethitha, "Unsteady flow of collapsible tube under transverse magneto hydrodynamic fluid," *International Journal of Advanced Science and Technology*, pp. 1995–2001, 2020.
- [9] M. Z. Ullah, D. Abuzaid, M. Asma, and A. Bariq, "Couple stress hybrid nanofluid flow through a converging-diverging channel," *Journal of Nanomaterials*, vol. 2021, Article ID 2355258, 13 pages, 2021.
- [10] H. P. Kok, E. N. K. Cressman, W. Ceelen et al., "Heating technology for malignant tumors: a review," *International Journal of Hyperthermia*, vol. 37, no. 1, pp. 711–741, 2020.
- [11] K. Loganathan, N. Alessa, R. Jain, F. Ali, and A. Zaib, "Dynamics of heat and mass transfer: ree-eyring nanofluid flow over a riga plate with bioconvection and thermal radiation," *Frontiers in Physics*, vol. 10, p. 990, 2022.
- [12] M. Ferdows, M. Shamshuddin, S. O. Salawu, and S. Sun, "Thermal cooling performance of convective nonnewtonian nanofluid flowing with variant power-index across moving extending surface," *Scientific Reports*, vol. 12, no. 1, pp. 8714–8720, 2022.
- [13] K. A. M. Alharbi, A. Ullah, N. Fatima et al., "Impact of viscous dissipation and coriolis effects in heat and mass transfer analysis of the 3d non-Newtonian fluid flow," *Case Studies in Thermal Engineering*, vol. 37, Article ID 102289, 2022.
- [14] F. Ali, K. Loganathan, S. Eswaramoorthi, M. Faizan, E. Prabu, and A. Zaib, "Bioconvective applications of unsteady slip flow over a tangent hyperbolic nanoliquid with surface heating: improving energy system performance," *International Journal of Algorithms, Computing and Mathematics*, vol. 8, no. 6, p. 276, 2022.
- [15] D. Rizk, A. Ullah, S. Elattar et al., "Impact of the kkl correlation model on the activation of thermal energy for the hybrid nanofluid (go+ znO+ water) flow through permeable vertically rotating surface," *Energies*, vol. 15, no. 8, p. 2872, 2022.
- [16] S. Khan, M. M. Selim, A. Khan, A. Ullah, T. Abdeljawad, and Ikramullah, M. Ayaz and W. K. Mashwani, "On the analysis of the non-Newtonian fluid flow past a stretching/shrinking permeable surface with heat and mass transfer," *Coatings*, vol. 11, no. 5, p. 566, 2021.
- [17] F. Ali, T. A. Kumar, and K. Loganathan, "Irreversibility analysis of cross fluid past a stretchable vertical sheet with mixture of carboxymethyl cellulose water based hybrid nanofluid," *Alexandria Engineering Journal*, vol. 64, 2022.
- [18] F. Ali, K. Loganathan, S. Eswaramoorthi, K. Prabu, A. Zaib, and D. K. Chaudhary, "Heat transfer analysis on carboxymethyl cellulose water-based cross hybrid nanofluid flow with entropy generation," *Journal of Nanomaterials*, vol. 2022, Article ID 5252918, 11 pages, 2022.
- [19] O. T. Bafakeeh, K. Raghunath, F. Ali et al., "Hall current and soret effects on unsteady mhd rotating flow of second-grade fluid through porous media under the influences of thermal

- radiation and chemical reactions,” *Catalysts*, vol. 12, no. 10, p. 1233, 2022.
- [20] C. S. Reddy, F. Ali, K. Al-Farhany, and W. Sridhar, “Numerical analysis of gyrotactic microorganisms in mhd radiative eyring-powell nanofluid across a static/moving wedge with sores and dufour effects,” *ZAMM Journal of Applied Mathematics and Mechanics/Zeitschrift für Angewandte Mathematik und Mechanik*, vol. 102, no. 11, Article ID e202100459, 2022.
- [21] C. Srinivas Reddy, F. Ali, and M. F. A. F. Ahmed, “Aspects on unsteady for mhd flow of cross nanofluid having gyrotactic motile microorganism due to convectively heated sheet,” *International Journal of Ambient Energy*, vol. 43, no. 1, pp. 6028–6040, 2022.
- [22] F. Ali, C. S. Reddy, N. Summayya, and M. F. Ahmed, “Effect of nonlinear thermal radiation on unsteady mhd flow of Maxwell nanofluid over a porous vertical sheet with chemical reaction,” *Heat Transfer*, vol. 50, no. 8, pp. 8259–8279, 2021.
- [23] F. Ali and N. Summayya, “Numerical simulation of cattaneo-christov double-diffusion theory with thermal radiation on mhd eyring-powell nanofluid towards a stagnation point,” *International Journal of Ambient Energy*, vol. 43, no. 1, pp. 4939–4949, 2022.
- [24] A. Ullah, M. M. Selim, M. M. Selim et al., “A magnetite-water-based nanofluid three-dimensional thin film flow on an inclined rotating surface with non-linear thermal radiations and couple stress effects,” *Energies*, vol. 14, no. 17, p. 5531, 2021.
- [25] Z. Shah, P. Kumam, A. Ullah, S. N. Khan, and M. M. Selim, “Mesoscopic simulation for magnetized nanofluid flow within a permeable 3d tank,” *IEEE Access*, vol. 9, pp. 135 234–135 244, 2021.
- [26] N. N. Reddy, V. S. Rao, and B. R. Reddy, “Chemical reaction impact on mhd natural convection flow through porous medium past an exponentially stretching sheet in presence of heat source/sink and viscous dissipation,” *Case Studies in Thermal Engineering*, vol. 25, Article ID 100, 2021.
- [27] B. Prabhakar Reddy and O. D. Makinde, “Numerical study on mhd radiating and reacting unsteady slip flow past a vertical permeable plate in a porous medium,” *International Journal of Ambient Energy*, vol. 43, no. 1, pp. 6007–6016, 2021.
- [28] A. F. Elelany, N. S. Elgazery, and R. Ellahi, “Blood flow of mhd non-Newtonian nanofluid with heat transfer and slip effects: application of bacterial growth in heart valve,” *International Journal of Numerical Methods for Heat and Fluid Flow*, vol. 30, 2020.
- [29] M. F. Ahmed, A. Zaib, F. Ali et al., “Numerical computation for gyrotactic microorganisms in mhd radiative eyring-powell nanomaterial flow by a static/moving wedge with Darcy-forchheimer relation,” *Micromachines*, vol. 13, no. 10, p. 1768, 2022.
- [30] S. O. Salawu, A. M. Obalalu, and M. Shamshuddin, “Non-linear solar thermal radiation efficiency and energy optimization for magnetized hybrid Prandtl-eyring nanofluid in aircraft,” *Arabian Journal for Science and Engineering*, vol. 48, no. 3, pp. 3061–3072, 2022.
- [31] S. Odejide, Y. Aregbesola, and O. Makinde, “Fluid flow and heat transfer in a collapsible tube,” *Romanian Journal of Physics*, vol. 53, pp. 499–506, 2008.
- [32] M. Gnanaswara Reddy, K. Venugopal Reddy, and O. Makinde, “Hydromagnetic peristaltic motion of a reacting and radiating couple stress fluid in an inclined asymmetric channel filled with a porous medium,” *Alexandria Engineering Journal*, vol. 55, no. 2, pp. 1841–1853, 2016.
- [33] R. Kodi and O. Mopuri, “Unsteady mhd oscillatory casson fluid flow past an inclined vertical porous plate in the presence of chemical reaction with heat absorption and sores effects,” *Heat Transfer*, vol. 51, no. 1, pp. 733–752, 2022.
- [34] N. C. Wawira, M. Kinyanjui, and K. Giterere, “Hydromagnetic non-Newtonian fluid flow in a convergent conduit,” *Journal of Applied Mathematics*, vol. 2022, Article ID 8131528, 13 pages, 2022.
- [35] M. Ferdows and Q. M. Al-Mdallal, “Effects of order of chemical reaction on a boundary layer flow with heat and mass transfer over a linearly stretching sheet,” *American Journal of Fluid Dynamics*, vol. 2, no. 6, pp. 89–94, 2013.
- [36] V. Ojiambo, M. Kinyanjui, and M. Kimathi, “A study of two-phase Jeffery Hamel flow in a geothermal pipe,” *International Journal of Advances in Applied Mathematics and Mechanics*, 2018.
- [37] M. A. Sattar, “Derivation of the similarity equation of the 2-D unsteady boundary layer equations and the corresponding similarity conditions,” *American Journal of Fluid Dynamics*, vol. 3, no. 5, p. 135, 2013.
- [38] A. Raptis, “Flow of a micropolar fluid past a continuously moving plate by the presence of radiation,” *International Journal of Heat and Mass Transfer*, vol. 41, no. 18, pp. 2865–2866, 1998.
- [39] A. Raptis, “Radiation and viscoelastic flow,” *International Communications in Heat and Mass Transfer*, vol. 26, no. 6, pp. 889–895, 1999.
- [40] D. Pal and S. Chatterjee, “Soret and Dufour effects on MHD convective heat and mass transfer of a power-law fluid over an inclined plate with variable thermal conductivity in a porous medium,” *Applied Mathematics and Computation*, vol. 219, no. 14, pp. 7556–7574, 2013.
- [41] L. F. Shampine, L. F. Shampine, I. Gladwell, and S. Thompson, *Solving ODEs with Matlab*, Cambridge University Press, Cambridge, UK, 2003.